International Journal of Applied Earth Observations and Geoinformation 117 (2023) 103222

Contents lists available at ScienceDirect

International Journal of Applied Earth Observation and Geoinformation

journal homepage: www.elsevier.com/locate/jag

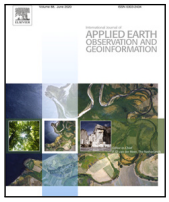

# Vertical land motion monitored with satellite radar altimetry and tide gauge along the Texas coastline, USA, between 1993 and 2020

Xiaojun Qiao [a,b], Tianxing Chu [a,b,*], Philippe Tissot [b,c], Ibraheem Ali [b], Mohamed Ahmed [c]

[a] Department of Computing Sciences, Texas A&M University-Corpus Christi, Ocean Drive 6300, Corpus Christi, TX 78412, USA
[b] Conrad Blucher Institute for Surveying and Science, Texas A&M University-Corpus Christi, Ocean Drive 6300, Corpus Christi, TX 78412, USA
[c] Department of Physical and Environmental Sciences, Texas A&M University-Corpus Christi, Ocean Drive 6300, Corpus Christi, TX 78412, USA

ARTICLE INFO

*Keywords:*
Coastal vertical land motion
Time-series reconstruction
Sea-level difference
Tide gauge
Radar altimetry

ABSTRACT

It is crucial nowadays to accurately monitor vertical land motion (VLM) near coasts and understand its spatial and temporal variability to quantify its impact to water-land interactions. This study developed and employed a double difference (DD) network adjustment method to reconstruct daily VLM time series and estimate their trends using sea-level observations recorded at 24 tide gauge (TG) stations located on the Texas coastline between 1993 and 2020. Based on the first difference between TG and the satellite radar altimetry (SRA) observations, the method calculated DD between correlated TG pairs to mitigate sea-level variations. Then all potential connections of TG pairs across the 24 stations were combined to form a TG network regarding the DD values. On a daily basis, the DD values reflected relative elevation difference for a specific connection and the network could be solved via weighted least squares to reconstruct elevations (i.e., VLM time series) at different TG stations. Results indicated that at most TG stations, clear VLM patterns were restored and found to be largely consistent with time series derived from continuously-operating global navigation satellite system (cGNSS). In addition, greater than 80% of the TG stations used in the work showed a linear VLM trend with an uncertainty of less than or equal to 1.0 mm/yr. The proposed DD network adjustment method provides long and continuous VLM time-series results, and has a potential to complement other geodetic techniques, particularly along the coastal areas where TG stations were densely installed.

## 1. Introduction

Continuous global sea-level rise, together with storm surge and heavy rainfall events, spells frequent flood risks and poses growing threats to the safety of near-shore infrastructures, resilience of coastal ecosystems, and marine habitats (Douglas et al., 2000). Rising seas also adversely impact quality of life and economic success of coastal residents around the world who live in low-lying coastal zones (McGranahan et al., 2007). It was reported that the frequency of high tide flooding (HTF), occurring when coastal water levels overshoot 0.5 m above the mean higher high water (MHHW) level, has doubled since 2000 along the U.S. coastlines (Sweet et al., 2019). Due to this trend of HTF, it is of crucial importance to keep track of sea level changes, model its spatial and temporal patterns, and apply pertinent knowledge in decision-making processes.

Sea-level measurements have long been recorded by tide gauge (TG) stations, some of which have started to function since the 19th century in a self-recording manner (Matthäus, 1972). A TG station is a land-attached device that integrates a set of monitoring sensors to observe and record the relative water-land movement. Specifically, it continuously measures and records the height of sea level relative to a vertical datum (Adebisi et al., 2021), referred to as relative sea-level change (RSLC). In coastal areas, RSLC collectively combines the effects of vertical land motion (VLM) and absolute sea-level change (ASLC). VLM reflects elevation changes of land surface in the form of either subsidence or uplift (Wöppelmann and Marcos, 2016). Different from RSLC, ASLC is not influenced by the local VLM and refers to the height variations of the ocean surface.

Recent advances in the investigation of coastal land subsidence disclosed that VLM can be estimated indirectly with sea-level difference between RSLC and ASLC data, particularly by using TG and satellite radar altimetry (SRA) observations. For nearly three decades, SRA technique has provided a wide spectrum of essential parameters such as ASLC variations calculated by measuring sea surface height (SSH) changes above a reference ellipsoid (Adebisi et al., 2021). The potential of estimating land subsidence with the difference between the variables of ASLC and RSLC has been explored (Cazenave et al., 1999; Qiao et al.,

* Correspondence to: 6300 Ocean Drive, Unit 5799, Corpus Christi, TX 78412, USA.
*E-mail address:* tianxing.chu@tamucc.edu (T. Chu).

https://doi.org/10.1016/j.jag.2023.103222
Received 8 September 2022; Received in revised form 1 February 2023; Accepted 2 February 2023
Available online 7 February 2023

2021). However, the VLM results may be contaminated by residuals of sea-level variations contained in the direct difference method. The limitation of the direct sea-level difference stems from bias drifts, intra- and inter-mission biases (Rezvani et al., 2021; Watson et al., 2015; Leuliette et al., 2004), spatial proximity between a TG and its corresponding altimeter footprint (Douglas et al., 2000; Nerem and Mitchum, 2002; Rezvani et al., 2022), complex responses of radar pulses to coastal zones (Adebisi et al., 2021; Xu et al., 2019), and so forth.

To improve the performance of VLM trend estimate with TG and SRA measurements, Kuo et al. developed an effective method that yielded less uncertainty by connecting a network of contributing TGs (Kuo et al., 2004). In essence, the method applied double difference to obtain relative land motion rate, $\Delta V\dot{L}M$, between any paired TGs (indexed by subscripts 1 and 2) as shown in Eq. (1):

$$\Delta V\dot{L}M = (A\dot{S}LC_1 - R\dot{S}LC_1) - (A\dot{S}LC_2 - R\dot{S}LC_2) \quad (1)$$

$$= (A\dot{S}LC_1 - A\dot{S}LC_2) - (R\dot{S}LC_1 - R\dot{S}LC_2) \quad (2)$$

where the $\cdot$ superscripts denotes temporal trends of VLM, ASLC, and RSLC. In Eq. (1), the first difference was made between the variables of RSLC and ASLC at individual TGs, and a further difference was conducted based on the first difference results between a pair of TGs indexed by subscripts 1 and 2. Finally the best VLM estimate at each TG was adjusted in the TG network regarding the $\Delta V\dot{L}M$ values with a stochastic model (Kuo et al., 2004).

In recent years, growing attention has been paid to the double difference estimator with different techniques for VLM estimate, primarily using TG stations with long observation history (De Biasio et al., 2020; Letetrel et al., 2015; Santamaría-Gómez et al., 2014). Current state of the art tends to determine linear RSLC and/or ASLC trends before conducting double difference and network adjustment for VLM trend estimate, therefore sea-level data with long observation history (e.g., > four decades) are favorable for mitigating trend estimation errors due to impacts made by low-frequency (e.g., decadal) sea-level fluctuations (Douglas, 1991). Nevertheless, it was reported that only approximately 35% of global TGs possess observing length of over four decades (Wöppelmann and Marcos, 2016) for robust sea-level change estimation. In addition, the reconstruction of VLM time series has been ignored in the past. Qiao et al. proposed a double difference-based method to estimate VLM time series for TG stations along the Texas Coast (Qiao et al., 2022). Sea-level variability was mitigated by coupling with well-correlated TG candidate(s) with record length of over 25 years. TG stations with record length of less than 25 years were ignored regardless of their potential in mitigating sea-level variability.

This study aims at exploring the knowledge of regional VLM estimates with sea-level observations acquired between 1993 and 2020 at multiple TG locations along the Texas coastline, a leading subsiding area across the U.S. coasts. A method of double difference and network adjustment was proposed and employed to discover VLM knowledge using TG and SRA observations, particularly along coastlines where other geospatial techniques such as, interferometric synthetic aperture radar (In-SAR), and light detection and ranging (LiDAR) may experience large-scale observation outages. Different from prior studies, this article addresses the following aspects:

(a). Calculation of double difference with TG and SRA data for a common length of observation history without special assumptions such as an identical ASLC rate for neighboring TGs.
(b). Constructing a TG network that consists of a series of paired TG stations, conducting least squares network adjustment on a daily basis, restoring VLM time series, and estimating VLM trend at any TG stations that have observation record history of over ten years between 1993 and 2020. This is a substantively generalized method to a previously published work (Qiao et al., 2022).
(c). Considering correlation coefficients between paired TG stations as weighting factors to control TG network geometry and compute VLM time series from daily TG network.

## 2. Study area and datasets

### 2.1. Study area

The Texas Coastline stretches 591 km from the Lower Rio Grande Valley past Galveston to the Texas-Louisiana border along the Northern Gulf of Mexico coastline, which is composed of the coastal regions of South Texas, Southeast Texas, and Texas Coastal Bend. This study focused on the Texas Gulf Coast region due to its continuously observed land subsidence at some locations (Fig. 1). For example, the Houston–Galveston area has experienced an excessive amount of VLM due to groundwater withdrawal, which has been extensively investigated in prior studies (Kasmarek et al., 2009; Kearns et al., 2015). Activities related to oil and/or gas extraction are also significant around the coastal region in Texas, which were believed to contribute to land deformation (Khorzad, 1999; Qu et al., 2015; Haley et al., 2022).

### 2.2. Data

#### 2.2.1. Tide gauge

TG records along the Texas coastline were accessed from the tides and currents website of National Oceanic and Atmospheric Administration (NOAA). Specifically, the mean value of 6-minute or 60-minute observations (depending on the data availability) in a day was calculated for daily water level (i.e., RSLC time series), at each station that had an observation record history of over ten years between January 1993 and March 2020. There was a total of 27 stations that fulfilled this criterion and, therefore, adopted in the TG dataset. It should be noted that TG observations of the station 8772440 (numerical identity at NOAA) were combined with that of TG 8772447, given that the two stations are located 0.8 km apart off an open channel near Freeport, TX, displaying consistent tidal characteristics. These two TG stations had an observation overlap between September 28, 2006, and March 19, 2008. After the combination of these two TGs, 26 TG stations remained for subsequent processing and analysis. Because the study mainly focused on reconstructing VLM time series and the corresponding trend based on relative water-level measurements, the mean value of the entire water-level record was removed from its daily observations at each TG station. Distribution of all TG stations employed in the study is shown in Fig. 1.

#### 2.2.2. Satellite altimetry

The ASLC measurements were obtained from the global sea surface height product within AVISO+ (https://www.aviso.altimetry.fr/), which are currently distributed by the Copernicus Marine Environment Monitoring Service (CMEMS) (E.U. Copernicus Marine Service Information, 2022). The ASLC data are the most frequently used SSH product and have been reported to have better correlation with TG data globally compared with other alternatives (Wöppelmann and Marcos, 2016). More specifically, the global gridded level-4 SSH product (i.e., SEALEVEL_GLO_PHY_L4_MY_008_047) from January 1993 to March 2020, along the Texas coastline, was accessed. The product was interpolated both spatially and temporally with its level-3 along-track product, where dynamic atmospheric corrections (DAC) has been included (E.U. Copernicus Marine Service Information, 2022). Spatial resolution of the level-4 product reached 0.25 × 0.25-degree, and in each grid cell sea-level anomalies were provided at a daily interval relative to a two-decade mean between 1993 to 2012.

#### 2.2.3. GNSS

GNSS measurements from 16 stations along coastal regions of Texas before the end of 2020 were used as ground truth to evaluate the performance of VLM estimate developed in the study. Fig. 1 illustrates the distribution of cGNSS stations in close proximity to the corresponding TGs along the Texas coastline. Specifically, positioning results of the station P036 were accessed from the Harris-Galveston Subsidence

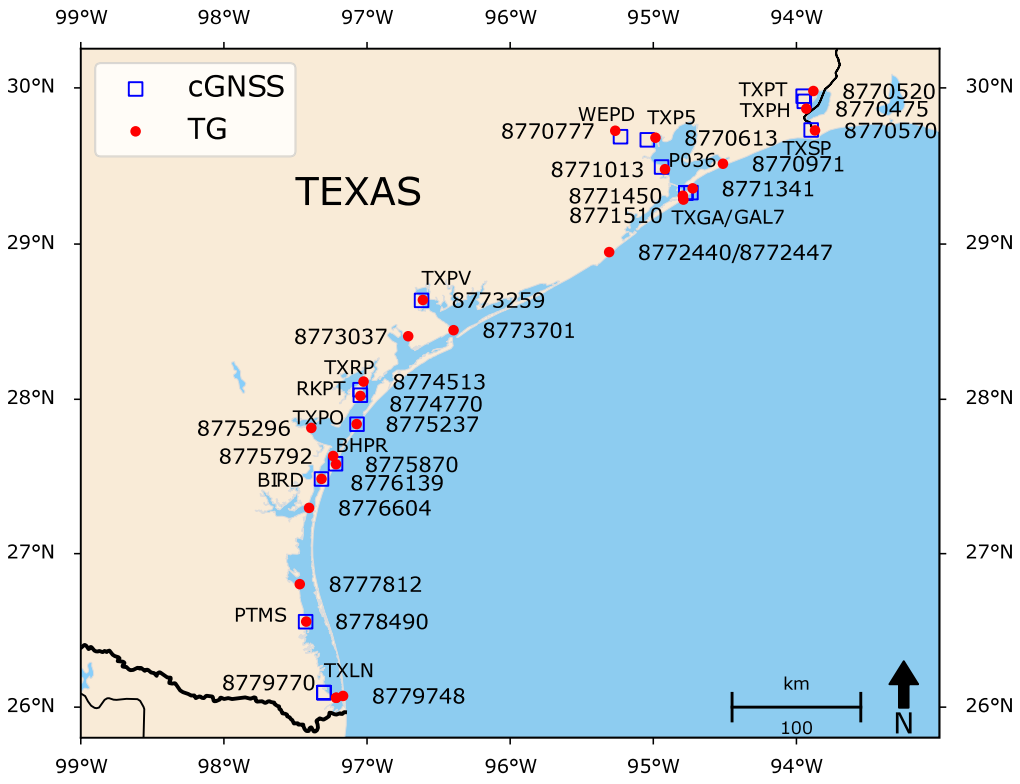


**Fig. 1.** Distribution of TG stations (marked to the side of red points with seven-digital numbers named by NOAA) and cGNSS stations (marked to the side of blue boxes with four-letter names) along the Texas coastline in the United states.

District (HGSD) (H.G.S.D., 2022). P036 was a station from the Port-A-Measure (PAM) network established by HGSD. GNSS antennas were routinely mounted on PAM poles attached to the ground 4 to 6 m below the surface, continuously collected data up to one to two weeks per month, and then rotated among other PAM sites (Zilkoski et al., 2003). This study also employed four cGNSS stations (i.e., RKPT, BHPR, BIRD, and PTMS) that were part of the coastal monitoring systems maintained by the Conrad Blucher Institute for Surveying and Science (CBI) at Texas A&M University-Corpus Christi (TAMU-CC). The Receiver Independent Exchange Format (RINEX) files from these four stations were accessed and downloaded to achieve cm-level accuracy with the precise point positioning (PPP) technique. And positioning solutions for the remaining cGNSS stations could directly be accessed through the Nevada Geodetic Laboratory (Blewitt et al., 2018). Daily positioning results can be derived from all cGNSS stations, depending on the data availability. It is worth noting that some cGNSS stations with short distance in space and inadequate overlap of observations over time were merged into one single virtual cGNSS site to form longer time series for validation purposes.

## 3. Method

### 3.1. Single difference

Conceptually, rates of ASLC changes $\dot{A}$ and RSLC changes $\dot{R}$ satisfy (Kuo et al., 2004):

$$\dot{U} = \dot{A} - \dot{R} \tag{3}$$

where $\dot{U}$ is the VLM rate. The time-series expression of Eq. (3) can be rewritten as:

$$U_i(t) = A_i(t) - R_i(t) \tag{4}$$

where $t$ stands for the continuous time, $U_i(t)$ and $R_i(t)$ depict VLM and RSLC variables, respectively, at a TG station indexed by $i$, and $A_i(t)$ represents the ASLC variable at an SRA observation grid cell that is in closest proximity to the TG station. Eq. (4) reflects the single difference (SD) between TG and SRA measurements at a specific TG site. In this study, Eq. (5) was adopted to compensate DAC for TG measurements and to calculate VLM time series from SD

$$U_i(t) = A_i(t) - \left[R_i(t) - D_i(t)\right] \tag{5}$$

where $D_i(t)$ represents the daily DAC value to correct sea-level variations in TG measurement.

### 3.2. Double difference between paired TGs

Moving one step further from the SD operation, double difference (DD) can be made between the observation values of any potential paired TG stations within a TG network along with corresponding SRA grid cell values. Let $B_{ij}(t)$ be the relative elevation difference between two paired TG stations, defined below:

$$B_{i,j}(t) = U_i(t) - U_j(t) \tag{6}$$

$$= \left[A_i(t) - R_i(t) - D_i(t)\right] - \left[A_j(t) - R_j(t) - D_j(t)\right] \tag{7}$$

where $U_i(t)$ and $U_j(t)$ are the elevations at paired TG stations indexed by $i$ and $j$, which can be computed via Eq. (5). More description of paired TG stations is introduced in Section 3.3.

### 3.3. TG network

Any two TG stations are considered forming a pair during the entire study period (i.e., between 1993 and 2020), provided that their full sea-level time series are highly correlated. A poor correlation between two TG stations does not warrant a pair. Within a set of TG stations, a network can be constructed by connecting all paired TG stations. Ideally, any potential two TG stations within the study area can be paired in a fully connected network as demonstrated in Fig. 2(a).

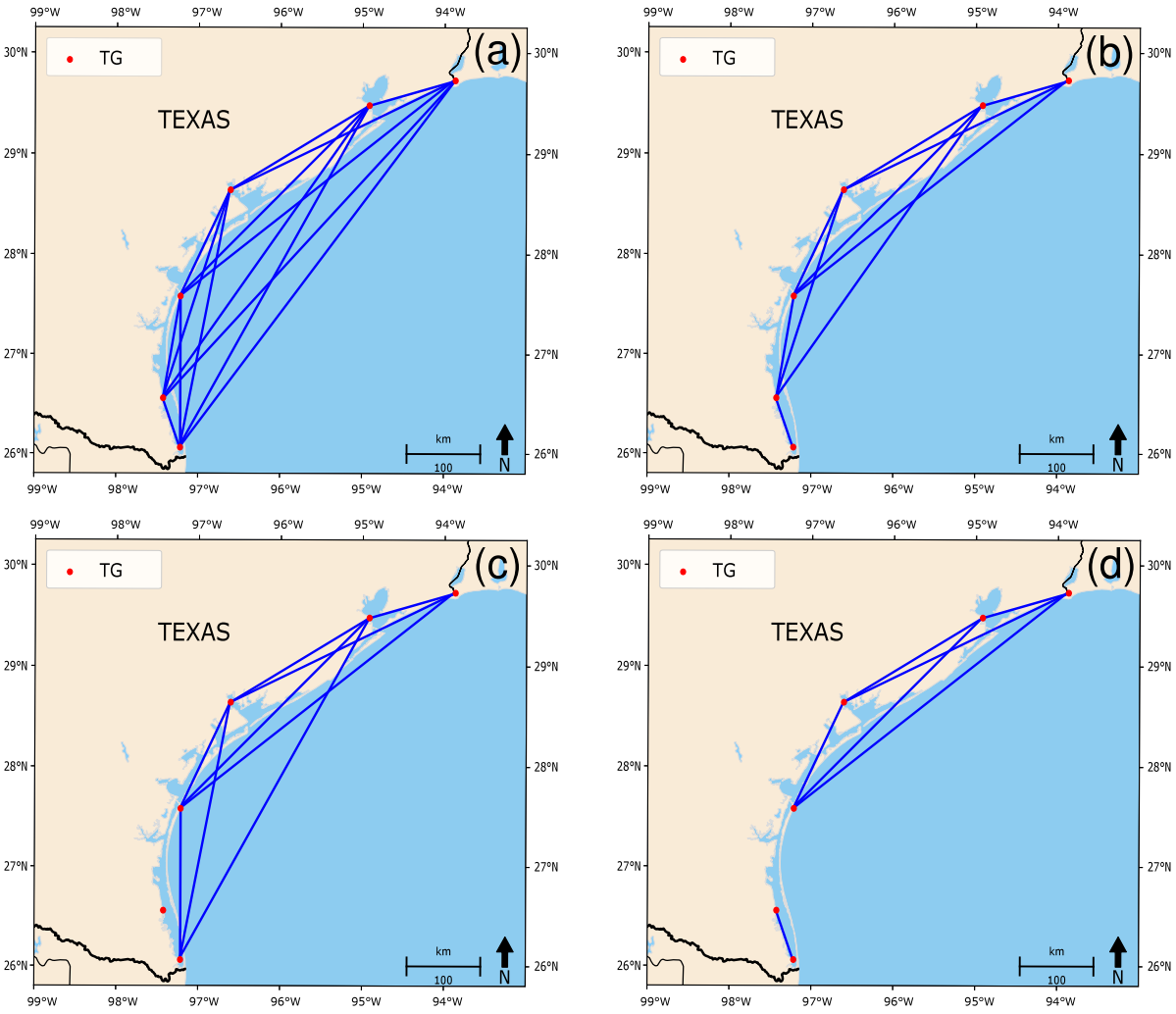


**Fig. 2.** Illustration of possible TG network examples. Without loss of generality, only six stations are chosen for display to avoid visual clutter. A blue line connecting two TG stations, marked in red dots, indicates a successful pair in the network. In case any two TG stations are found uncorrelated or there is an observation outage between them examined on a daily basis, they are not paired by the blue line. Assume there are a total of $k$ TG stations within the study area, and the number of active TG stations within the network per day is $m$. (a) Any two TG stations are paired in the fully connected network across all $k$ TG stations. In this case $m = k$ with all $k$ stations being active within the network; (b) All TG stations are connected to the network although one or more stations are considered weakly connected. In this case $m = k$; (c) In case there are $p$ TG stations not connected to the remaining stations, $m = k - p$; and (d) The TG network is made up with several smaller parts and $m = 0$ for this particular date without further processing.

However, poor correlations may occur, reducing the number of paired connections in the network. Moreover, the network is also adaptive dependent on TG observation availability within a pair on a per day scale. For instance, although two TG stations (e.g., A and B) are considered paired, their connection is supposed to be excluded from the network at a particular time $t$ in case of an observation outage at either station A or B. Fig. 2(b), (c), and (d) demonstrate reduced connections within a network due to: (1) poor correlation between two TG stations analyzed with their full lengths of sea-level data during the entire study period, and/or (2) a lack of available sea-level data examined on a daily basis. It is important to note that only six TG stations are displayed in Fig. 2 in order to avoid visual clutter with blue line connections. Assume there are a total of $k$ TG stations within the study area, and the number of active TG stations within the network per day is $m$. In both Fig. 2(a) and (b), $m = k$ because all TG stations are connected into the network despite difference in network connectivity. In case there are $p$ TG stations not connected to any other stations (e.g., $p = 1$ in Fig. 2(c)), these stations are not part of the network and $m = k - p$. Furthermore, in case the TG network is made up with several smaller parts (Fig. 2(d)), subsequent processing is terminated due to lack of constraints between different parts and, therefore, the number of active TG stations $m = 0$ for this particular time.

### 3.4. VLM time series reconstruction

As opposed to prior studies that primarily adopted one constant TG network during the entire study period to analyze and model VLM trends, this study adopted an adaptive TG network on a daily basis to reconstruct the VLM time series (Fig. 2(a), (b), and (c)). Let $B_{ij}(t)$ be the double difference between any possible combination of two paired stations in a TG network at a specific time $t$. The mathematical construction of the TG network can be modeled as matrix $\mathbf{B}(t)$ as shown in Eq. (8):

$$\mathbf{B}(t) = \begin{bmatrix} 0 & B_{1,2}(t) & B_{1,3}(t) & \cdots & B_{1,m-1}(t) & B_{1,m}(t) \\ 0 & 0 & B_{2,3}(t) & \cdots & B_{2,m-1}(t) & B_{2,m}(t) \\ \vdots & \vdots & \vdots & \ddots & \vdots & \vdots \\ 0 & 0 & 0 & \cdots & 0 & B_{m-1,m}(t) \\ 0 & 0 & 0 & \cdots & 0 & 0 \end{bmatrix} \tag{8}$$

where each element above the diagonal in the matrix is computed using Eq. (7), the subscripts of each element suggest the indices of paired TG stations, and $m$ is the number of active stations in a TG network at time $t$.

The next step is to restore elevation estimates at time $t$ at all $m$ active TGs in a network, i.e., $u = \left[U_1(t), U_2(t), \ldots, U_m(t)\right]^T$ containing

$m$ unknown elevation variables, from a series of calculated double difference $B_{ij}(t)$ in a TG network. The problem is modeled to solving a linear system:

$$\begin{bmatrix} 1 & -1 & 0 & \cdots & 0 & 0 \\ 1 & 0 & -1 & \cdots & 0 & 0 \\ \vdots & \vdots & \vdots & \ddots & \vdots & \vdots \\ 0 & 0 & 0 & \cdots & 1 & -1 \end{bmatrix}_{l\times m} \cdot \begin{bmatrix} U_1(t) \\ U_2(t) \\ \vdots \\ U_m(t) \end{bmatrix} + \begin{bmatrix} \varepsilon_1 \\ \varepsilon_2 \\ \vdots \\ \varepsilon_l \end{bmatrix} = \begin{bmatrix} B_{1,2}(t) \\ B_{1,3}(t) \\ \vdots \\ B_{m-1,m}(t) \end{bmatrix}_{l\times 1} \tag{9}$$

where $l$ represents the number of all possible TG pairs corresponding to $B_{i,j}(t)$ elements in matrix $\mathbf{B}(t)$ and $\tilde{\varepsilon} = [\varepsilon_1, \varepsilon_2, \ldots, \varepsilon_l]^T$ is the white noise residual error. Eq. (9) can be simplified as:

$$\tilde{A}u + \tilde{\varepsilon} = \tilde{b} \tag{10}$$

where $\tilde{A}$ is design matrix of the linear system and vector $\tilde{b} = \left[B_{1,2}(t), B_{1,3}(t), \ldots, B_{i,j}(t), \ldots, B_{m-1,m}(t)\right]^T$ stores $l$ values of $B_{i,j}(t)$ between any valid TG pairs.

In Eq. (10), $rank(\tilde{A}) = m - 1$ holds because not all the matrix $\tilde{A}$ columns are linearly independent (Meyer, 2000). It needs an external constraint to solve the rank-deficient linear least-squares problem. To make the system uniquely solvable, an initial VLM time series calculated from a TG station with a long observation history was incorporated as a constraint. Specifically, an additional row was appended to Eq. (10) as defined below:

$$\begin{bmatrix} \tilde{A} \\ c \end{bmatrix} \cdot u + \begin{bmatrix} \tilde{\varepsilon} \\ \varepsilon_c \end{bmatrix} = \begin{bmatrix} \tilde{b} \\ h(t) \end{bmatrix} \tag{11}$$

where $c$ is the appended row vector to the designed matrix $\tilde{A}$ with 1 placed at the column index corresponding to the TG station serving as the constraint and remaining elements being 0. For example, $c = [1, 0, \ldots, 0]$ if the first TG station is selected as the constraint. The variable $\varepsilon_c$ is the residual error at the appending row, and $h(t)$ is the initial VLM value at time $t$ for the constraint TG station. Specifically, $h(t)$ is expressed as (Qiao et al., 2022):

$$h(t) = \left\{ A(t) - \frac{1}{q}\sum_{i=1}^{q}\left[A_{Q_i}(t) - f_{Q_i}(t)\right] \right\} - \left\{ R(t) - D(t) - \frac{1}{q}\sum_{i=1}^{q}\left[R_{Q_i}(t) - D_{Q_i}(t) - g_{Q_i}(t)\right] \right\} \tag{12}$$

where $A(t)$, $R(t)$, and $D(t)$ are the time series of the variables of ASLC, RSLC, and DAC respectively at the constraint TG station. $A_{Q_i}(t)$ and $R_{Q_i}(t)$ represent the ASLC and RSLC time series at TG stations, $Q = \{Q_1, Q_2, \ldots, Q_q\}$, and $q$ is the number of elements contained in the set $Q$. The stations within the set $Q$ are those correlated with the constraint TG with long observation history. Variables $f_{Q_i}(t)$ and $g_{Q_i}(t)$ represent the linear regression functions for ASLC and RSLC time series after DAC removal, respectively, at the TG station $Q_i \in Q$. In essence, to estimate $h(t)$, Eq. (12) mitigates sea-level variability of the constraint TG by coupling with well-correlated TG stations in the vicinity. And Eq. (11) can be simplified as:

$$Au + \varepsilon = b \tag{13}$$

Considering elements in vector $\tilde{b}$ were calculated based on multiple TG pairs, the correlation coefficient of each TG pair was utilized as the weight in each row of the linear system when reconstructing daily VLM time series. Specifically, a $(l+1)\times(l+1)$ diagonal weight matrix, $W$, was used in the linear system. The first $l$ diagonal elements in $W$ are correlation coefficients calculated with daily RSLC time series after DAC correction between the paired TGs corresponding to $B_{i,j}(t)$, and the last diagonal element regarding the constraint was set to an empirical value of 0.5. Finally, with a full rank design matrix $A$, the vector $u$ in Eq. (13) is solved with unbiased weighted least squares (Kutner et al., 2004) of an overdetermined system by minimizing the $L^2$-norm of $\varepsilon$:

$$\hat{u} = argmin\|W^{1/2}(b - Au)\|_2 = (A^T W A)^{-1} A^T W b \tag{14}$$

where $\hat{u}$ contains estimated elevations at all $m$ active TG stations at time $t$.

**Table 1**
Noise models for trend estimation in Hector.

| | Models | Description |
|---|---|---|
| 1 | WN | White Noise |
| 2 | PLWN | Power-Law + White Noise |
| 3 | FNWN | Flicker Noise + White Noise |
| 4 | GGMWN | Generalized Gauss–Markov + White Noise |
| 5 | RWFNWN | Random Walk + FNWN |
| 6 | AR(1) | ARMA(1, 0) first-order autoregressive |

### 3.5. GNSS processing

The absolute positioning method, such as precise point positioning (PPP), models GNSS error propagation and estimates positions from a single receiver. In PPP technique, precise GNSS orbit and clock data are corrected through a network of regional/global reference stations (Choy et al., 2017). Among PPP implementations, GNSS-inferred positioning system and orbit analysis simulation software (GIPSY-OASIS), developed by the Jet Propulsion Laboratory (JPL), has become a popular software suite and found to give more coherent and accurate results compared with the OPUS utility (Wang et al., 2017). In this study, JPL's GipsyX-1.7 package (Bertiger et al., 2020), a recent GIPSY-OASIS replacement, was adopted to process raw pseudorange and carrier phase data collected at the cGNSS stations maintained by TAMU-CC's CBI as stated in Section 2.2.3. During PPP processing, the ionosphere exchange (IONEX) files were used for the second-order ionospheric corrections, the global pressure and temperature (GPT2) model was considered for tropospheric correction, and ocean-tide loading corrections using the global ocean tide (GOT-4.8) model were included. PPP solutions were offered in an Earth-Centered-Earth-Fixed (ECEF) coordinate system with X, Y, and Z coordinates, which were then transformed to north, east, and up (ENU) directions.

### 3.6. Trend estimation

Offsets, outliers, missing data, and residual seasonal variations will inherently exist in VLM time series obtained in both DD-based and GNSS, which negates linear regression methods for the purpose of reliable trend estimation. Hector, a scientific tool for estimating robust linear trends from time series data with temporal correlated noises, was used to fit the VLM time series with various noise-combination models (Bos et al., 2013). Table 1 lists six noise models, $N = \{$WN, PLWN, FNWN, GGMWN, RWFNWN, AR(1)$\}$, that were used in this study. The optimal noise model that best fits the VLM time series was decided based on Akaike Information Criterion (AIC) and Bayes Information Criterion (BIC) (Bos et al., 2019), defined as:

$$O = argmin(AIC_n + BIC_n), n \in N \tag{15}$$

where $O$ is the optimal noise, with which the VLM linear trend and uncertainty can then be determined.

## 4. Results

### 4.1. Sea-level difference analysis

Fig. 3 illustrates an example of TG and SRA observation comparison at the TG station 8771450 located at Pier 21, Galveston, TX. Five years of observation data between January 1, 1993, and December 31, 1997 are highlighted to facilitate visualizing the details of seasonal changes. TG and SRA measurements agreed well, in general, in terms of the seasonal variations, and DAC greatly reduced the sea-level fluctuations in the TG measurements. It can be observed that TG measurements had stronger high-frequency variations in the sea-level observations than that in SRA measurements. This is because TG data were recorded every six minutes or hourly by NOAA (Shu et al., 2021; Douglas et al., 2000),

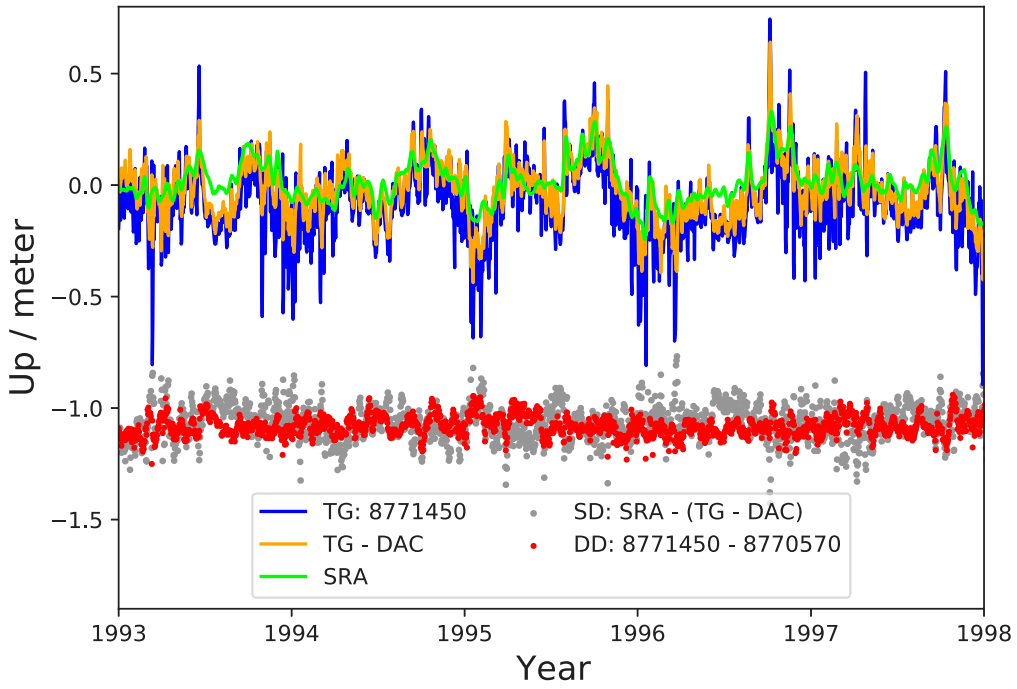


**Fig. 3.** TG and SRA time series comparison at TG station 8771450 located at Pier 21, Galveston, TX, between January 1, 1993, and December 31, 1997. It also shows the VLM results estimated with the SD and DD methods.

and then averaged to daily in this study. However, the level-4 SRA product was interpolated to daily values from its level-3 product, where revisit periods with any available SRA platforms were no sooner than ten days (Douglas et al., 2000).

In addition, the amplitude of semi-annual/annual cycles of TG observations tended to stay periodically greater than that of the SRA measurements. These low-frequency differences between TG and SRA measurements were also documented in other studies (Vinogradov and Ponte, 2010; Etcheverry et al., 2015). Several major factors may be held responsible for this phenomenon. First, maximum water-level amplitude may not be captured in a timely fashion due to the limited temporal resolution of SRA. Second, the SRA product used in the study was generated by interpolating its level-3 along-track SSH observations from different altimter platforms, which smoothed water levels over time and space (Pujol et al., 2016). Third, tidal corrections have been applied in the level-3 SRA product (E.U. Copernicus Marine Service Information, 2022), while daily tidal variability was removed only by averaging daily TG measurements.

Due to the aforementioned high-frequency and low-frequency differences between TG and SRA data in observing water-level changes, the SD method left the VLM time series prone to noises when calculating differential values between the TG and SRA measurements. On the other hand, the DD method outperformed the SD method because the former could further reduce noises by differentiating the SD results with that of its pair. In Fig. 3, both SD and DD time series were vertically shifted with an arbitrary amount to clearly highlight VLM results, and this did not alter the nature of the main focus on VLM estimate. Fig. 4 displays the periodicity in the VLM results obtained from the SD method at TG station 8771450 (Pier 21, Galveston, TX) and DD method between TG stations 8771450 and 8775870 (Bob Hall Pier, Corpus Christi, TX). In the SD periodogram, differences between TG and SRA observations are clearly characterized by half-month cycles due to the infrequent revisit period of SRA and the semi-annual pattern due to the periodical amplitude offsets. However, the periodicity at frequencies of half and six months were not identified in the DD periodogram. Meanwhile, the signal power of the DD results was suppressed for frequencies less than half month, meaning that the DD method tends to be less prone to high-frequency sea-level variations after differentiating the TG and SRA measurements.

### 4.2. Initial VLM time series of h(t) at the constraint TG station

TG station of 8771450 (Pier 21, Galveston, TX) was employed as the constraint TG station to calculate the $h(t)$ time series because: (1) no missing TG observation outage was found during the entire investigation period between 1993 and 2020; and (2) the combined daily observations of its near-located cGNSS stations (i.e., GAL7 and TXGA) make up around 80% coverage of the entire investigation period from 1993 to 2020, facilitating validation between $h(t)$ and cGNSS time series results.

Four other TG stations, $Q$ = {8770570, 8771013, 8774770, 8775870}, were selected as correlated TG stations per Eq. (12). These four stations were selected because a correlation coefficient of greater than 0.90 was achieved between each of them and the TG station 8771450. In Fig. 5, results of $h(t)$ were compared against the combined vertical time series processed from cGNSS stations GAL7 and TXGA. The distances from the TG station 8771450 to the cGNSS stations TXGA and GAL7 are approximately 2.9 and 5.9 km, respectively. It should be noted that the TXGA results (marked in orange color) were vertically shifted relative to the GAL7 results (marked in yellow color) for visualization purposes. This could be justified by the fact that: (1) cGNSS time series of GAL7 and TXGA stations were based on different origins of local ENU coordinate systems, and (2) the nature of VLM trend prior to and after the cGNSS gap was not impacted. Some abrupt vertical offsets from the cGNSS station TXGA can be noticed (enlarged in Fig. 6), which was due to reported human intervention such as changes related to the elevation cut-off angle or antenna (Blewitt et al., 2018). Nevertheless, Fig. 5 demonstrates overall consistent trends between $h(t)$ and cGNSS time series.

To further examine the validity of the initial VLM time series, Hector software utility was used to estimate monthly mean $h(t)$ trend vs. that obtained from the cGNSS vertical time series. Hector is adept at processing time series with offsets as shown in the combined GAL7 and TXGA data (Fig. 5). Fig. 6 shows the model that was fitted to the cGNSS vertical time series, and the estimated linear cGNSS trend was $-4.3\pm0.3$ mm/yr. On the contrary, $h(t)$ yielded a $-4.9\pm0.5$ mm/yr linear trend. Therefore, well within the precision range, a trend difference of approximately 0.6 mm/yr was achieved in terms of VLM trend estimate.

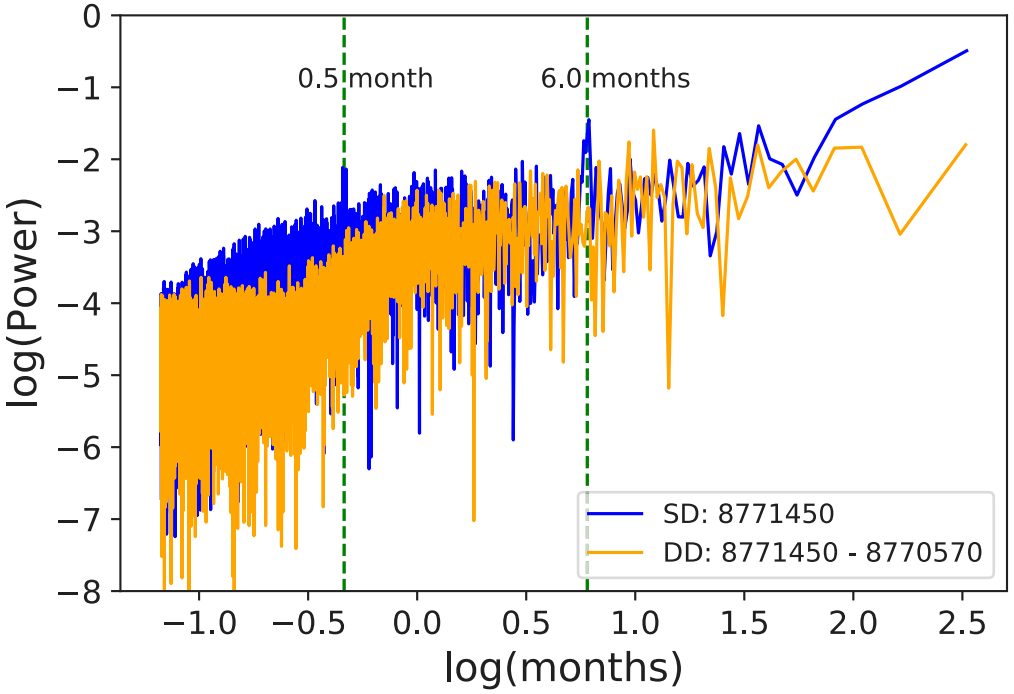


**Fig. 4.** Periodogram of using SD method at a TG station 8771450 (Pier 21, Galveston, TX) and DD method between TG stations 8771450 and 8775870 (Bob Hall Pier, Corpus Christi, TX). The green dashed lines correspond to the half month and semi-annual periodicity.

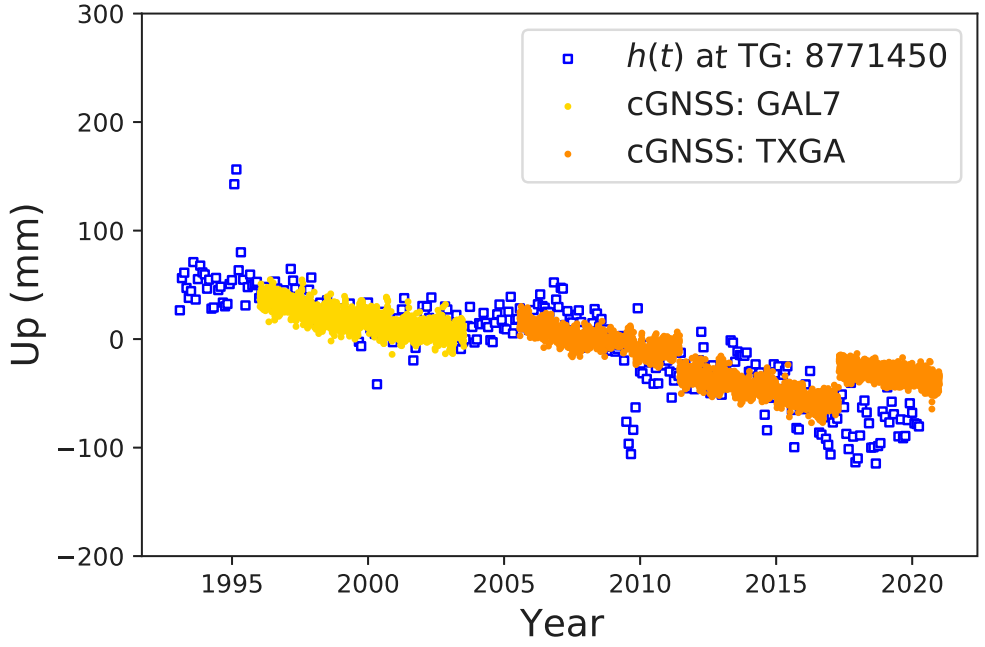


**Fig. 5.** Results of $h(t)$ compared against cGNSS vertical time series at the near-located GAL7 and TXGA cGNSS stations, with cGNSS time-series shifted vertically for visual purposes. The distances from the TG station 8771450 to the cGNSS stations TXGA and GAL7 are approximately 2.9 and 5.9 km, respectively. A short GNSS observation gap occurred between the TXGA and GAL7 stations. The TXGA results (marked in orange color) were vertically shifted relative to the GAL7 results (marked in yellow color) for visualization purposes. (For interpretation of the references to color in this figure legend, the reader is referred to the web version of this article.)

### *4.3. Reconstruction of VLM time series*

Correlation coefficients were calculated for all possible combinations among the 26 TG stations using their entire lengths of RSLC time series (Fig. 7) to acquire valid TG pairs in the daily network. Considering the overall good correlation among the TG stations along the Texas coastline, a correlation coefficient threshold of 0.80 was adopted to form the daily network within which paired TG stations were strongly correlated. In other words, this threshold was used to shape the daily network by dropping connections between any two TG stations within which correlation coefficient fell below 0.80. The value of the correlation coefficient threshold (i.e., 0.80) is a compromised choice in achieving the goal of pairing highly correlated TG stations while avoiding an ill-posed network as shown in Fig. 2(d). TGs 8770971 and 8777812 were further excluded in the study given their overall low correlation. Thus, 24 TG stations remained and were used for the reconstruction of VLM time series and trend estimation via the DD network adjustment method.

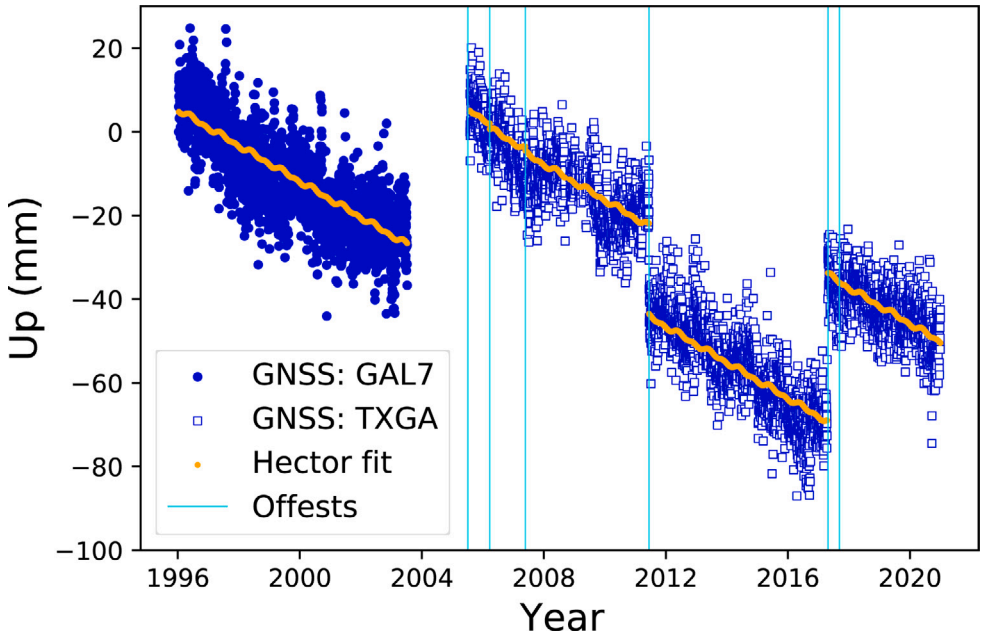


**Fig. 6.** Hector fitted model and trend estimation for the combined cGNSS vertical time series (i.e., the GAL7 and TXGA cGNSS stations) near the TG station 8771450.

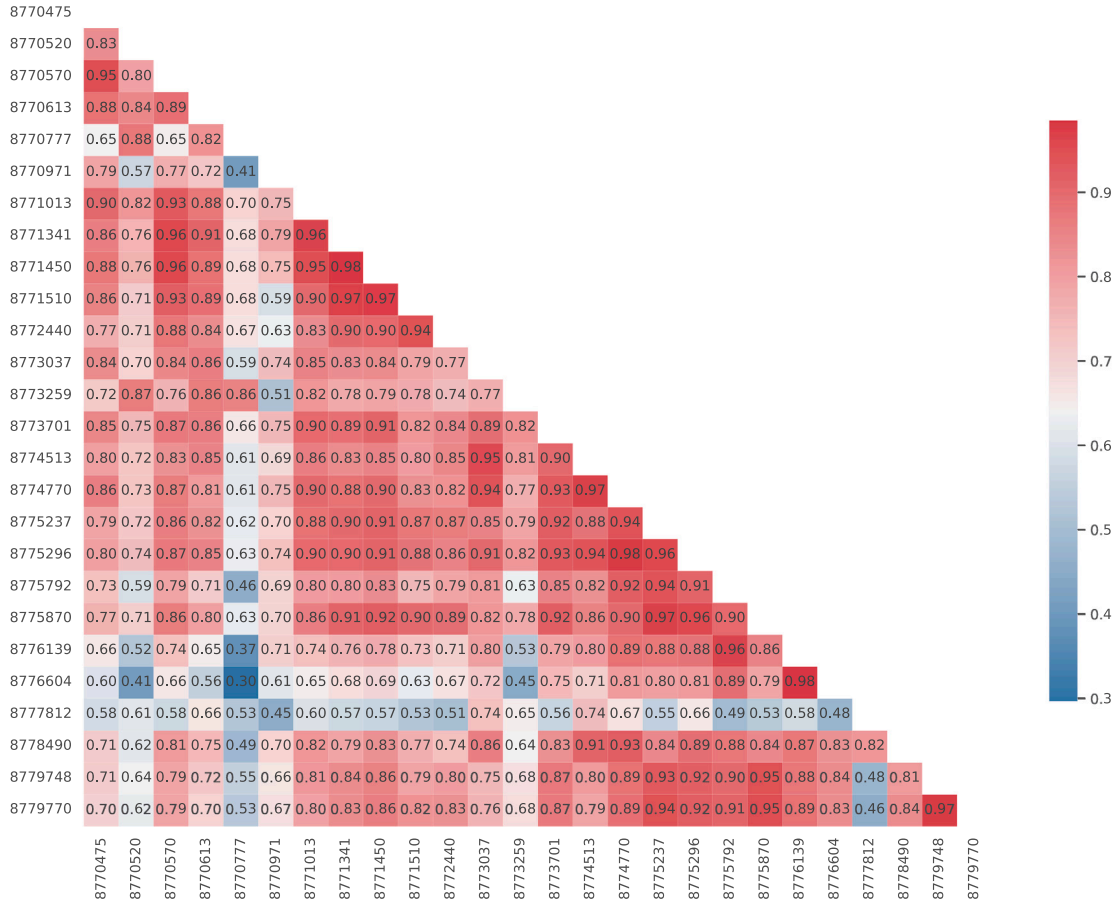


**Fig. 7.** Correlation coefficients for all combinations among the 26 TG stations involved in the study using their entire lengths of RSLC time series.

On a daily basis, $B_{i,j}(t)$ was calculated for each TG pair using Eq. (7) when the TG observations were available and the corresponding correlation coefficient was greater than 0.80. The matrix $\mathbf{B}(t)$ was then converted to a linear system as shown in Eq. (9). It should be noted that all-zero columns in matrix $\tilde{A}$, corresponding to the scenario shown in Fig. 2(c), as well as the corresponding unknown parameter $U_i(t)$ in $u$, were removed from the network due to unavailable TG observations or low correlation to any other TG stations at $t$. The linear system

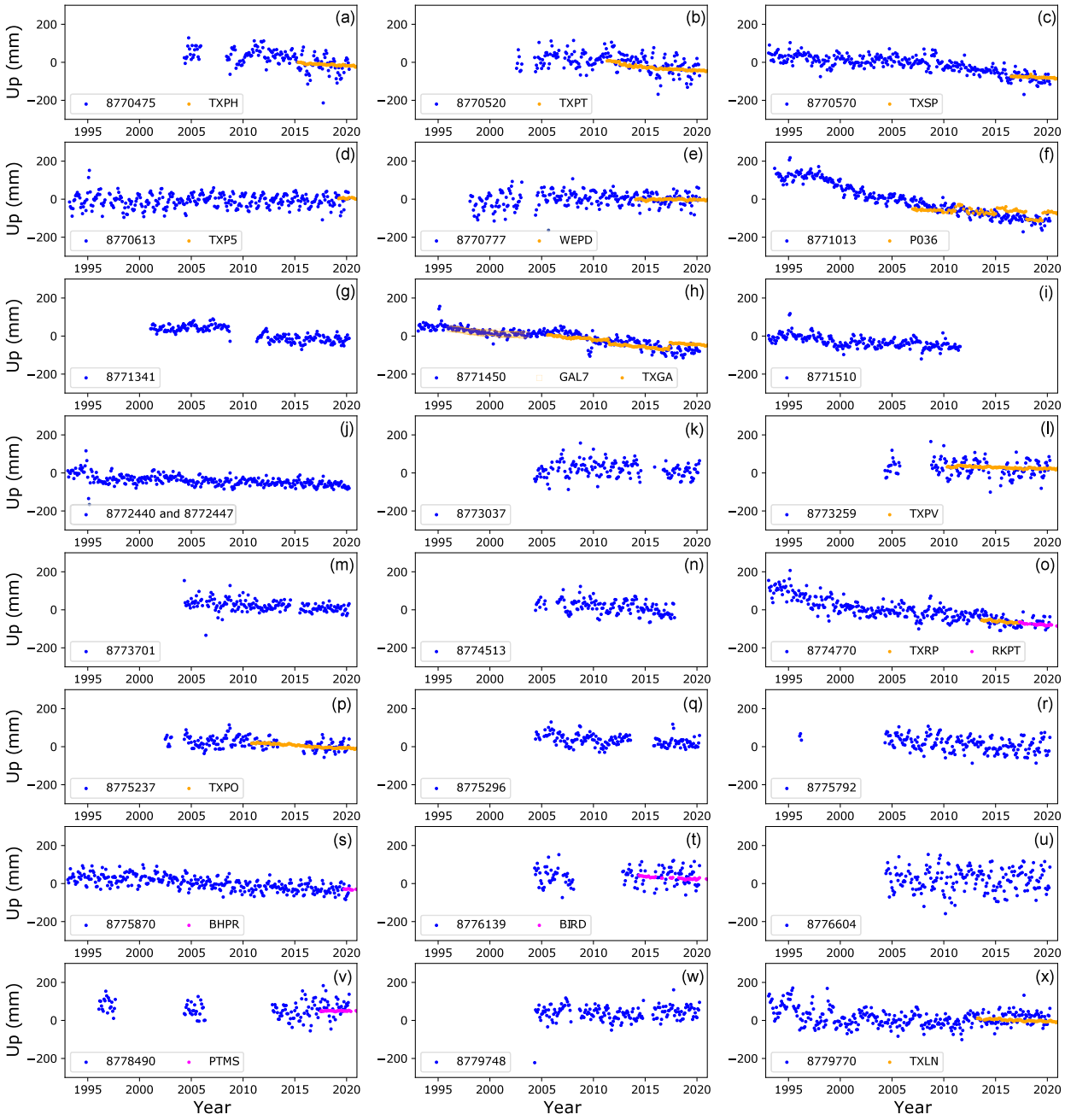


**Fig. 8.** Comparisons of monthly mean VLM time series obtained via the DD network adjustment method at 24 TG stations (marked with blue dots) and via near-located cGNSS stations (marked with magenta at CBI stations and yellow at other stations). (For interpretation of the references to color in this figure legend, the reader is referred to the web version of this article.)

in Eq. (13) after appending constraint $h(t)$ can be solved via weighted least squares per Eq. (14). By solving the linear system repeatedly over time, VLM time-series can be reconstructed from double-differenced sea-level measurements.

Fig. 8 illustrates the reconstructed monthly mean VLM time series at highlighted 24 TG stations as well as vertical positioning time series at the corresponding near-located cGNSS stations. Note monthly mean results were displayed as opposed to daily results in Fig. 8 to highlight long-term trends at those TG stations with better visual clarity. Clear VLM patterns with limited uncertainty can be observed at some TG stations such as 8770570, 8771013, and 8774770 in Fig. 8(c), (f), and (o), respectively. Some TG stations that had relatively shorter lengths of observation period could still reveal distinct VLM processes such as 8773259, 8773701, and 8774513 in Fig. 8(l), (m), and (n). In addition, results show that DD network adjustment method-based VLM time series were found consistent with that of the vertical GNSS positioning time series at most near-located cGNSS stations. GNSS, SD- and DD-based VLM time series were passed to Hector software utility, and their corresponding trend and uncertainty estimates are summarized in Table 2.

## 5. Discussion

To evaluate the overall performance of the VLM trend estimated with sea-level measurements at TG stations under investigation, the study compared the trend estimates made by the DD network adjustment method and the SD methods against that made at near-located cGNSS stations (Fig. 9). SD and DD-based trends exhibit consistent

**Table 2**
VLM results estimated at TG stations with the DD network adjustment and SD methods and at the corresponding near-located cGNSS stations. The units of SD, DD, and GNSS trends are mm/yr.

| TG | | | | | cGNSS | | | |
|---|---|---|---|---|---|---|---|---|
| Name | Longitude | Latitude | SD trend[a] | DD trend[a] | Name | Longitude | Latitude | GNSS trend[b] |
| 8770475 | −93.931° | 29.867° | −6.5 ± 1.7 | −5.6 ± 1.3 | TXPH | −93.945° | 29.915° | −3.1 ± 0.3 |
| 8770520 | −93.882° | 29.980° | −4.6 ± 1.5 | −3.8 ± 1.0 | TXPT | −93.953° | 29.947° | −5.3 ± 0.4 |
| 8770570 | −93.870° | 29.728° | −4.0 ± 0.8 | −4.8 ± 0.9 | TXSP | −93.897° | 29.731° | −2.2 ± 0.2 |
| 8770613 | −94.985° | 29.682° | 0.2 ± 0.4 | 0.1 ± 0.2 | TXP5 | −95.042° | 29.668° | −0.1 ± 1.3 |
| 8770777 | −95.266° | 29.726° | 0.0 ± 0.6 | 0.9 ± 1.1 | WEPD | −95.229° | 29.688° | −0.3 ± 0.4 |
| 8771013 | −94.918° | 29.480° | −10.0 ± 1.5 | −10.1 ± 0.6 | P036 | −94.920° | 29.494° | −2.6 ± 0.3 |
| 8771341 | −94.725° | 29.357° | −4.0 ± 1.6 | −4.3 ± 0.8 | TXGA[d] | −94.773° | 29.328° | −4.3 ± 0.3 |
| 8771450 | −94.793° | 29.310° | −4.3 ± 1.3 | −4.9 ± 0.5 | TXGA[d] | −94.773° | 29.328° | −4.3 ± 0.3 |
| 8771510 | −94.789° | 29.285° | −2.0 ± 0.5 | −3.1 ± 0.5 | TXGA[d] | −94.773° | 29.328° | −4.3 ± 0.3 |
| 8772440[c] | −95.308° | 28.948° | −1.6 ± 0.5 | −1.9 ± 0.2 | ~ | ~ | ~ | ~ |
| 8773037 | −96.712° | 28.407° | −0.7 ± 2.8 | −0.4 ± 1.5 | ~ | ~ | ~ | ~ |
| 8773259 | −96.610° | 28.641° | −1.8 ± 2.0 | −1.7 ± 0.6 | TXPV | −96.619° | 28.638° | −1.2 ± 0.3 |
| 8773701 | −96.396° | 28.446° | −3.3 ± 1.0 | −2.4 ± 0.4 | ~ | ~ | ~ | ~ |
| 8774513 | −97.024° | 28.114° | −4.8 ± 1.3 | −4.3 ± 0.8 | ~ | ~ | ~ | ~ |
| 8774770 | −97.047° | 28.022° | −5.8 ± 0.5 | −6.5 ± 1.0 | TXRP[e] | −97.049° | 28.062° | −4.2 ± 0.3 |
| 8775237 | −97.073° | 27.840° | −2.8 ± 0.8 | −2.0 ± 0.5 | TXPO | −97.070° | 27.840° | −3.1 ± 0.2 |
| 8775296 | −97.389° | 27.815° | −3.2 ± 1.5 | −2.4 ± 0.7 | ~ | ~ | ~ | ~ |
| 8775792 | −97.237° | 27.633° | −3.9 ± 0.8 | −3.0 ± 0.5 | ~ | ~ | ~ | ~ |
| 8775870 | −97.217° | 27.580° | −2.2 ± 1.2 | −3.0 ± 0.2 | BHPR | −97.220° | 27.583° | −1.1 ± 1.0 |
| 8776139 | −97.318° | 27.485° | −0.2 ± 1.1 | 0.5 ± 0.6 | BIRD | −97.318° | 27.484° | −2.7 ± 0.6 |
| 8776604 | −97.405° | 27.297° | 0.2 ± 3.1 | 0.3 ± 0.7 | ~ | ~ | ~ | ~ |
| 8778490 | −97.425° | 26.558° | −1.3 ± 0.6 | −0.8 ± 0.6 | PTMS | −97.429° | 26.557° | 0.1 ± 0.2 |
| 8779748 | −97.168° | 26.073° | −0.8 ± 0.5 | 0.2 ± 0.8 | ~ | ~ | ~ | ~ |
| 8779770 | −97.216° | 26.061° | −1.3 ± 1.0 | −1.7 ± 1.0 | TXLN | −97.301° | 26.095° | −2.3 ± 0.3 |

The ~ symbol represents unavailability of GNSS measurements.
[a]Trend was calculated with monthly mean VLM data.
[b]Trend was calculated with daily VLM time series.
[c]TG data of the station 8772447 was appended to that of the station 8772440.
[d]Observation data from The cGNSS station GAL7, located at (−94.737°, 29.330°), was combined with that of the station TXGA.
[e]Observation data from CBI cGNSS station RKPT, located, located at (−97.047°, 28.026°), was combined with that of the station TXRP.

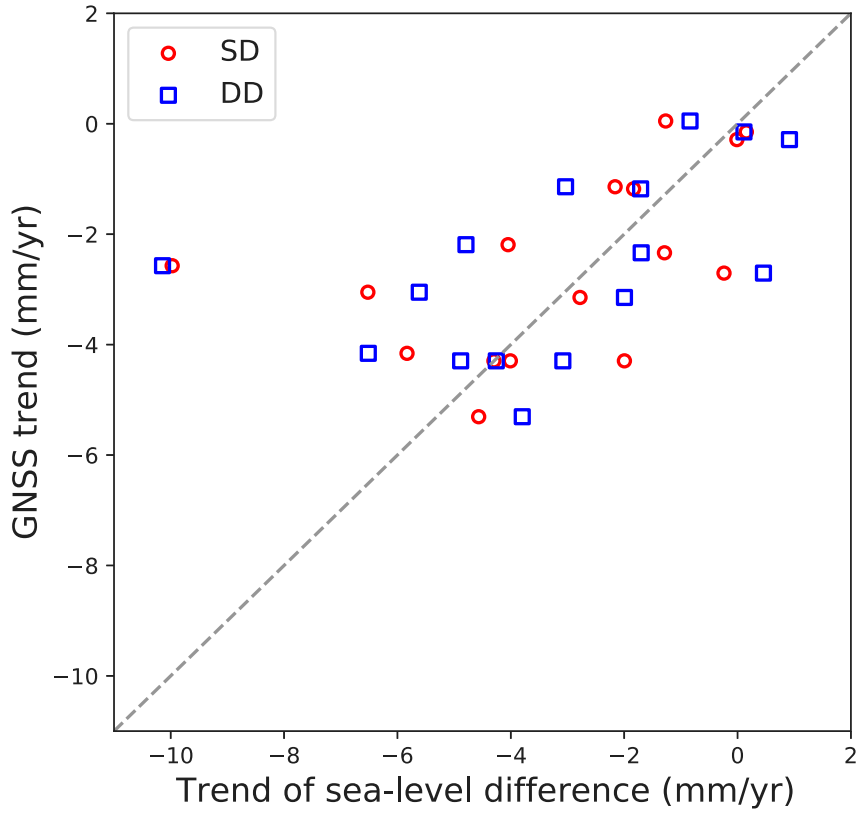


**Fig. 9.** VLM trend validation of SD and DD results by comparing with GNSS VLM estimate assumed to be ground truth.

performance with each other, reaching a correlation coefficient of 0.97. In the scatter plot, the diagonal 1:1 relationship line suggests complete agreement between two trend estimate methods. Most dots that represent SD vs. GNSS trend estimate and DD vs. GNSS trend achieved an overall agreement around the 1:1 relationship line. The correlation coefficients of SD vs. GNSS and DD vs. GNSS are 0.59 and 0.51, respectively. However, it is also documented that the VLM trend at one TG station with either SD or DD method was noticeably overestimated relative to the GNSS result (i.e., both the blue and red dots to the left of Fig. 9). This bias refers to the cGNSS station P036 and the TG named station 8771013, both located within San Leon, TX, city limits with an approximate distance of 2.8 km. Possible reasons for some points of deviation from the 1:1 line are:

(1) Short observation length of a cGNSS station may bias the GNSS-based trend estimate compared with that from a long and continuous history of TG measurements such as shown in Fig. 8(s), especially when the cGNSS stations fail to observe a non-linear subsiding period such as shown in Fig. 8(f) and (o). Besides, during data collection at GNSS P036, different antennas may be rotated and used for observation, which resulted in vertical shifts in the P036 time series as shown Fig. 8(f).
(2) Different trends may come at a TG and its near located cGNSS station as a result of the highly variable nature of the VLM pattern in space (e.g., the TG station 8779770 is approximately 9 km apart from the cGNSS station TXLN). The result comparison between DD and other space-geodetic techniques such as InSAR should be considered because the TG station may be found in close proximity with a corresponding InSAR pixel (e.g., within 10 m).
(3) In the DD network adjustment method, a TG station that paired with fewer stations indicates less observability and is, therefore, prone to higher variability in VLM estimate. For example, TG station 8776604 was paired to only a few stations, as shown in Fig. 7, and thus using it produced relatively noisy VLM results as released in Fig. 8(u).
(4) Some TG stations with relatively short-term observation (i.e., around ten years) were included in the study, which caused difficulties in accurate VLM trend estimate relative to the GNSS results. In addition, some TG stations experienced long periods of data outage, which exacerbated the accuracy of the VLM regression (Fig. 8(l), (t) and (v)).

Fig. 10 shows the comparison of yearly standard deviation (STD) based on the VLM results estimated with the SD and DD methods. Yearly data was calculated to illustrate the STD significance between using SD and DD methods within the time span in the study. It is obvious that the DD method significantly mitigated resultant VLM variations at most TG stations except 8776139, 8776604, and 8778490. In addition, it can be noticed that from the TG station 8776139 and subsequent subplots in Fig. 10, VLM variations were not well mitigated by the DD method as for other TG stations. One possible reason is that these TG stations stay relatively isolated along the South Texas coastline, which may have caused amplified temporal sea-level variations among these and other stations, resulting in comparatively poor observability obtained from a limited number of paired TG stations as indicated in Fig. 7. Moreover, compared with the SD method, the DD network adjustment method was also proved to be effective in reducing the VLM trend uncertainty (Fig. 11). From the bar plot, the number of TG stations whose trend uncertainty was greater than 1.0 mm/yr reduced from 13 in SD method to 4 in DD network adjustment method. Around 83% (20 out of 24) TG stations were reported to achieve a trend uncertainty of less than or equal to 1.0 mm/yr. The VLM trend uncertainty of the DD network adjustment method appears greater than that of the SD method at TG stations 8770570, 8770777, 8774770, and 8779748 (Fig. 11). Meantime, the DD method shows smaller STD than that obtained from the SD method at those stations (Fig. 10). This is potentially related to the significant difference in the VLM time series resulted from SD and DD methods, which led to different degrees of non-linearity before trend estimate. On the other hand, because the STD time series were calculated on a per-year basis, it mitigated, to some extent, the impact of the non-linearity of the VLM trend.

The selection of the weight value in the last element of matrix $W$ should largely be dependent on the way the $h(t)$ time series is evaluated. For instance, if $h(t)$ is estimated with reliable cGNSS results, a higher value close to one is suggested. On the other hand, a lower value should be selected if there is a lack of confidence in $h(t)$ estimate. However, a value close to zero should be avoided because this would result in an ill-conditioned linear system. In this article, an empirical value of 0.5 was selected as the weight value for $h(t)$ and the selection of this value needs further investigation. However, it should be noted that this value is supposed to have limited impact on solving the linear system, given that the length of the vector $\tilde{b}$ is generally much greater than that of $h(t)$ (i.e., $l$ vs. 1).

The reliability of the SRA data depends on the determination of fixed and time variable systematic errors, such as mission-specific bias drifts and intra/inter-mission biases, within and between each of available satellite altimeter missions (Watson et al., 2015; Rezvani et al., 2021). The fixed systematic error in SRA could largely be mitigated through daily DD calculation. Whereas the remainder of the systematic errors contained in the altimetry data were not particularly modeled in data processing. Therefore, the residual systematic errors that cannot be filtered by DD could still contaminate the results and need future investigation.

Last but not least, in the SD and DD network adjustment methods, the great-circle distance (i.e., the shortest distance between two points on the surface of the Earth) was adopted to pair a TG station and the center of its associated SRA grid cell. Land may be covered within the altimeter footprint and in the returned echo, which may degrade the validity of the sea surface height estimate due to the complex water-land interactions in coastal zones. For the level-4 SRA product used in the study, the influence of coastal land contamination has been partially taken care of by using waveform retracking technique (Vignudelli et al., 2011) and favorable data editing and tuning routines to guarantee the data quality during processing made from its L2p stage (Pujol and Mertz, 2019; CNES, 2017). However, noises related to land contamination may still be contained in the SRA product, which may cause uncertainty during the DD and/or SD VLM estimate. The accuracy and uncertainty impact of the SRA product contributed from coastal land contamination has been understudied in the past, and thus needs further investigation.

## 6. Conclusion

The study developed the method of double difference in network adjustment to reconstruct daily VLM time series and estimate the VLM trend with sea-level observations from 24 TG stations together with SRA data along the Texas coastline from 1993 to 2020. At most TG stations, the reconstructed VLM time series demonstrated clear temporal patterns and were found consistent with vertical coordinate time series obtained from corresponding near-located cGNSS stations. Regarding the VLM trend estimate, the DD network adjustment method agreed well with SD method with a high correlation of 0.97. While no significant difference in correlation was found when comparing the GNSS results with SD and DD trends (i.e., $R = 0.59$ and $R = 0.51$, respectively), the DD method effectively managed to reduce VLM variations using double differenced sea-level data within a TG network. Both yearly standard deviation and VLM trend uncertainty statistics at most TG stations with DD results were notably lower than that of the SD method. Processed with the DD network adjustment method, the trend uncertainty of VLM time series for greater than 80% of TG stations was found less than or equal to 1.0 mm/yr. Results of this

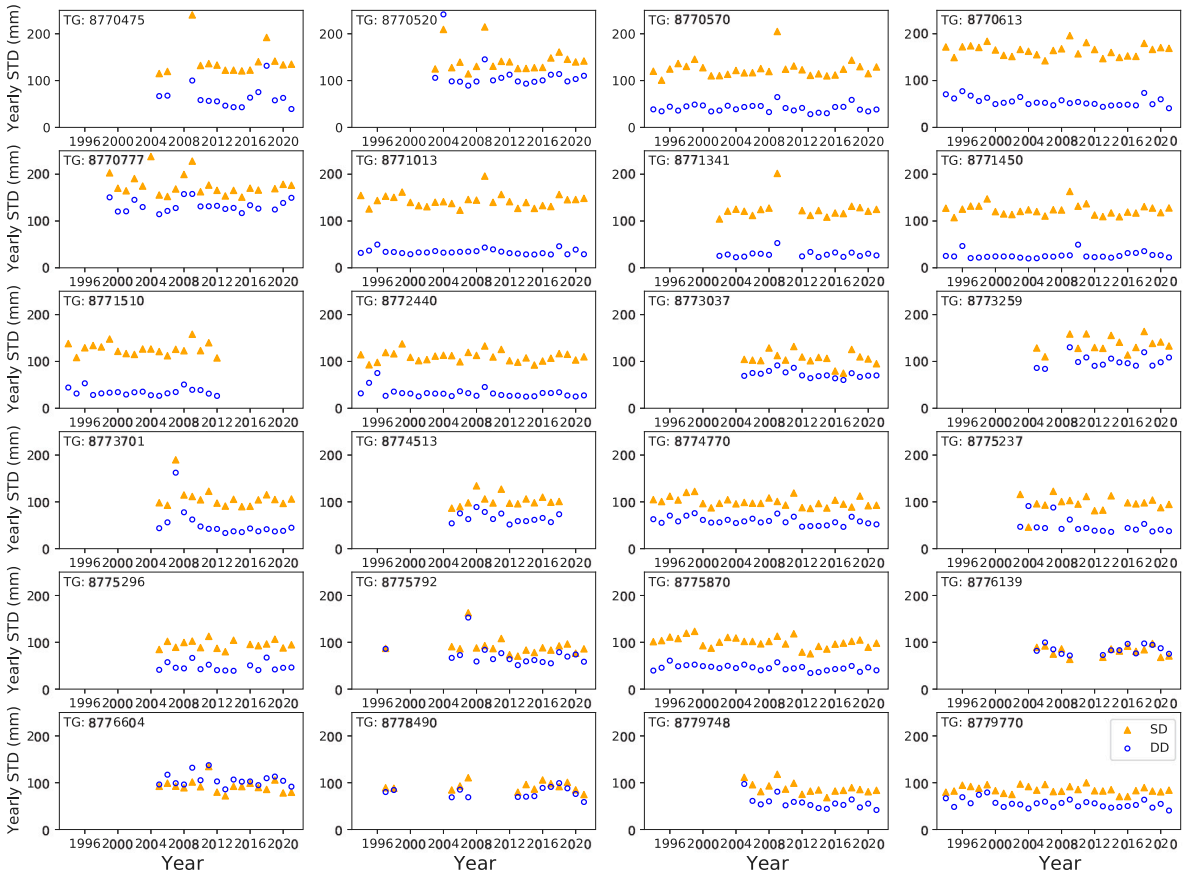


**Fig. 10.** Comparison of yearly standard deviation (STD) based on VLM results estimated with the SD and DD network adjustment methods.

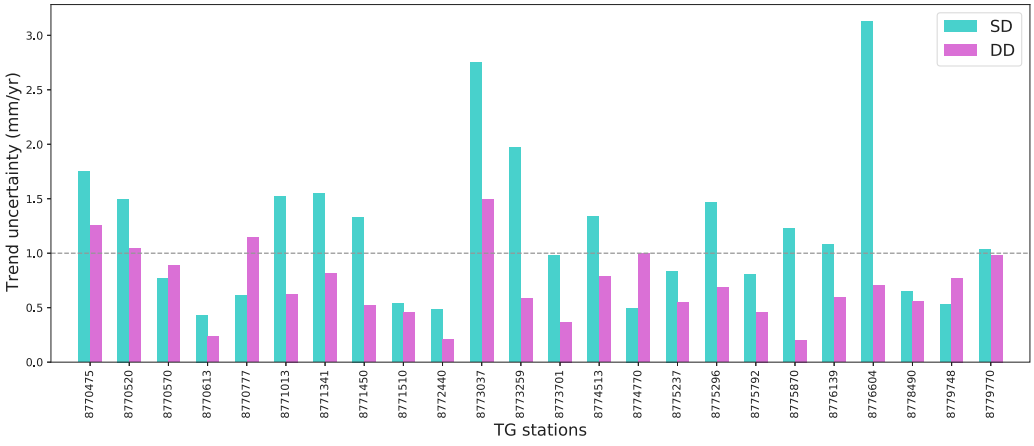


**Fig. 11.** Bar plot of the VLM trend uncertainties with the SD and DD network adjustment methods.

study manifested the feasibility of reconstructing VLM time series from the DD network adjustment method, which is significant to reveal the temporal processes of coastal land subsidence, even at TG stations with short record length of observation period (e.g., ten years). Being able to provide long and continuous results (up to nearly 30 years since 1993), this study demonstrates potential of sea-level observations of TG and SRA to complement popular geodetic techniques such as cGNSS and InSAR for revealing VLM knowledge, particularly along coastal areas where a dense network of TG stations were installed. The intended future work includes: (1) characterizing both spatial and temporal variability of VLM to further examine its patterns along the Texas coastline, (2) evaluating the developed method at other locations where VLM knowledge should be explored such as along semi-enclosed seas and large lakes, and (3) evaluating the impact of temporal resolution in the VLM time series results on the ability to restore linear and non-linear subsidence trends.

## CRediT authorship contribution statement

**Xiaojun Qiao:** Conceptualization, Methodology, Data curation, Validation, Formal analysis, Investigation, Writing – original draft, Writing – review & editing. **Tianxing Chu:** Formal analysis, Writing – original

draft. **Philippe Tissot:** Resources, Writing – review & editing. **Ibraheem Ali:** Writing – review & editing. **Mohamed Ahmed:** Writing – review & editing.

## Declaration of competing interest

The authors declare that they have no known competing financial interests or personal relationships that could have appeared to influence the work reported in this paper.

## Data availability

Data will be made available on request.

## Acknowledgments

This research was supported by the U.S. Department of Commerce-National Oceanic and Atmospheric Administration (NOAA), USA through the University of Southern Mississippi (USM) under the terms of Agreement [No. NA13NOS4000166]. The opinions expressed herein are those of the authors and do not necessarily reflect the views of NOAA or USM.

## References

Adebisi, N., Balogun, A.L., Min, T.H., Tella, A., 2021. Advances in estimating sea level rise: A review of tide gauge, satellite altimetry and spatial data science approaches. Ocean & Coastal Management 208, 105632.

Bertiger, W., Bar-Sever, Y., Dorsey, A., Haines, B., Harvey, N., Hemberger, D., Heflin, M., Lu, W., Miller, M., Moore, A.W., et al., 2020. GipsyX/RTGx, a new tool set for space geodetic operations and research. Adv. Space Res. 66 (3), 469–489.

Blewitt, G., Hammond, W.C., Kreemer, C., 2018. Harnessing the GPS data explosion for interdisciplinary science. EOS Trans. Am. Geophys. Union 99 (10.1029), 485.

Bos, M., Fernandes, R., Bastos, L., 2019. Hector User Manual Version 1.7. 2. Space and Earth Geodetic Analysis Laboratory, Covilhã, Portugal.

Bos, M., Fernandes, R., Williams, S., Bastos, L., 2013. Fast error analysis of continuous GNSS observations with missing data. J. Geod. 87 (4), 351–360.

Cazenave, A., Dominh, K., Ponchaut, F., Soudarin, L., Cretaux, J., Le Provost, C., 1999. Sea level changes from Topex-Poseidon altimetry and tide gauges, and vertical crustal motions from DORIS. Geophys. Res. Lett. 26 (14), 2077–2080.

Choy, S., Bisnath, S., Rizos, C., 2017. Uncovering common misconceptions in GNSS Precise Point Positioning and its future prospect. GPS Solut. 21 (1), 13–22.

CNES, 2017. Along-Track Level-2+(L2P) SLA Product Handbook. CNES, Paris, France.

De Biasio, F., Baldin, G., Vignudelli, S., 2020. Revisiting vertical land motion and sea level trends in the Northeastern Adriatic Sea using satellite altimetry and tide gauge data. J. Mar. Sci. Eng. 8 (11), 949.

Douglas, B.C., 1991. Global sea level rise. J. Geophys. Res.: Oceans 96 (C4), 6981–6992.

Douglas, B., Kearney, M.S., Leatherman, S.P., 2000. Sea Level Rise: History and Consequences. Elsevier.

Etcheverry, L.R., Saraceno, M., Piola, A.R., Valladeau, G., Möller, O., 2015. A comparison of the annual cycle of sea level in coastal areas from gridded satellite altimetry and tide gauges. Cont. Shelf Res. 92, 87–97.

E.U. Copernicus Marine Service Information, 2022, Global ocean gridded L4 sea surface heights and derived variables reprocessed (1993-ongoing). https://doi.org/10.48670/moi-00148.

Haley, M., Ahmed, M., Gebremichael, E., Murgulet, D., Starek, M., 2022. Land subsidence in the Texas Coastal bend: Locations, rates, triggers, and consequences. Remote Sens. 14 (1), 192.

H.G.S.D., 2022. Harris Galveston Subsidence District [online] URL https://hgsubsidence.org/. (Accessed 17 June 2022).

Kasmarek, M.C., Gabrysch, R.K., Johnson, M.R., 2009. Estimated Land-Surface Subsidence in Harris County, Texas, 1915–17 to 2001. US Department of the Interior, US Geological Survey.

Kearns, T.J., Wang, G., Bao, Y., Jiang, J., Lee, D., 2015. Current land subsidence and groundwater level changes in the Houston metropolitan area (2005–2012). J. Surv. Eng. 141 (4), 05015002.

Khorzad, K., 1999. Land subsidence along the Texas Gulf Coast due to oil and gas withdrawal. Environ. Geosci. 6 (3), 157.

Kuo, C., Shum, C., Braun, A., Mitrovica, J., 2004. Vertical crustal motion determined by satellite altimetry and tide gauge data in Fennoscandia. Geophys. Res. Lett. 31 (1).

Kutner, M.H., Nachtsheim, C.J., Neter, J., 2004. Applied Linear Regression Models, Vol. 4.

Letetrel, C., Karpytchev, M., Bouin, M.N., Marcos, M., Santamaría-Gómez, A., Wöppelmann, G., 2015. Estimation of vertical land movement rates along the coasts of the Gulf of Mexico over the past decades. Cont. Shelf Res. 111, 42–51.

Leuliette, E.W., Nerem, R.S., Mitchum, G.T., 2004. Calibration of TOPEX/Poseidon and jason altimeter data to construct a continuous record of mean sea level change. Mar. Geod. 27 (1–2), 79–94.

Matthäus, W., 1972. On the history of recording tide gauges. Proc. R. Soc. Edinburgh B 73, 26–34.

McGranahan, G., Balk, D., Anderson, B., 2007. The rising tide: assessing the risks of climate change and human settlements in low elevation coastal zones. Environ. Urbanization 19 (1), 17–37.

Meyer, C.D., 2000. Matrix Analysis and Applied Linear Algebra, Vol. 71. Siam.

Nerem, R., Mitchum, G., 2002. Estimates of vertical crustal motion derived from differences of TOPEX/POSEIDON and tide gauge sea level measurements. Geophys. Res. Lett. 29 (19), 1–4.

Pujol, M.I., Faugère, Y., Taburet, G., Dupuy, S., Pelloquin, C., Ablain, M., Picot, N., 2016. DUACS DT2014: the new multi-mission altimeter data set reprocessed over 20 years. Ocean Sci. 12 (5), 1067–1090.

Pujol, M., Mertz, F., 2019. Sea level TAC DUACS products.

Qiao, X., Chu, T., Tissot, P., Louis, J., 2021. Land subsidence with tide gauge, radar altimetry and GNSS: A case study at subsiding coast in Texas. In: Proceedings of the 34th International Technical Meeting of the Satellite Division of the Institute of Navigation. ION GNSS+ 2021, pp. 3956–3962.

Qiao, X., Chu, T., Tissot, P., Louis, J., Ali, I., 2022. Land subsidence estimation with tide gauge and satellite radar altimetry measurements along the Texas Gulf Coast, USA. IEEE Geosci. Remote Sens. Lett.

Qu, F., Lu, Z., Zhang, Q., Bawden, G.W., Kim, J.W., Zhao, C., Qu, W., 2015. Mapping ground deformation over Houston–Galveston, Texas using multi-temporal InSAR. Remote Sens. Environ. 169, 290–306.

Rezvani, M.H., Watson, C.S., King, M.A., 2021. Estimating vertical land motion and residual altimeter systematic errors using a Kalman-based approach. J. Geophys. Res.: Oceans 126 (6), e2020JC017106.

Rezvani, M.H., Watson, C.S., King, M.A., 2022. Vertical deformation and residual altimeter systematic errors around continental Australia inferred from a Kalman-based approach. J. Geod. 96 (12), 96.

Santamaría-Gómez, A., Gravelle, M., Wöppelmann, G., 2014. Long-term vertical land motion from double-differenced tide gauge and satellite altimetry data. J. Geod. 88 (3), 207–222.

Shu, S., Liu, H., Beck, R.A., Frappart, F., Korhonen, J., Lan, M., Xu, M., Yang, B., Huang, Y., 2021. Evaluation of historic and operational satellite radar altimetry missions for constructing consistent long-term lake water level records. Hydrol. Earth Syst. Sci. 25 (3), 1643–1670.

Sweet, W., Dusek, G., Carbin, G., Marra, J., Marcy, D., Simon, S., 2019. State of US high tide flooding with a 2020 outlook (vol. NOAA techn).

Vignudelli, S., Kostianoy, A.G., Cipollini, P., Benveniste, J., 2011. Coastal Altimetry. Springer Science & Business Media.

Vinogradov, S.V., Ponte, R.M., 2010. Annual cycle in coastal sea level from tide gauges and altimetry. J. Geophys. Res.: Oceans 115 (C4).

Wang, G., Turco, M., Soler, T., Kearns, T.J., Welch, J., 2017. Comparisons of OPUS and PPP solutions for subsidence monitoring in the greater Houston area. J. Surv. Eng. 143 (4), 05017005.

Watson, C.S., White, N.J., Church, J.A., King, M.A., Burgette, R.J., Legresy, B., 2015. Unabated global mean sea-level rise over the satellite altimeter era. Nature Clim. Change 5 (6), 565–568.

Wöppelmann, G., Marcos, M., 2016. Vertical land motion as a key to understanding sea level change and variability. Rev. Geophys. 54 (1), 64–92.

Xu, X.Y., Xu, K., Xu, Y., Shi, L.-W., 2019. Coastal altimetry: A promising technology for the coastal oceanography community. In: Estuaries and Coastal Zones-Dynamics and Response to Environmental Changes. IntechOpen.

Zilkoski, D.B., Hall, L.W., Mitchell, G.J., Kammula, V., Singh, A., Chrismer, W.M., Neighbors, R.J., 2003. The Harris–Galveston coastal subsidence district/national geodetic survey automated global positioning system subsidence monitoring project. In: Proceedings of the US Geological Survey Subsidence Interest Group Conference. US Geological Survey, pp. 13–28.